

See discussions, stats, and author profiles for this publication at: <https://www.researchgate.net/publication/242651752>

# Immobilizing Metal Nanoparticles to Metal-Organic Frameworks with Size and Location Control for Optimizing Catalytic Performance

ARTICLE in JOURNAL OF THE AMERICAN CHEMICAL SOCIETY · JUNE 2013

Impact Factor: 12.11 · DOI: 10.1021/ja403330m · Source: PubMed

---

CITATIONS

98

READS

206

## 3 AUTHORS, INCLUDING:



**Qilong Zhu**

National Institute of Advanced Industrial Sci...

43 PUBLICATIONS 662 CITATIONS

[SEE PROFILE](#)



**Qiang xu**

Hefei Union University

341 PUBLICATIONS 11,572 CITATIONS

[SEE PROFILE](#)

# Immobilizing Metal Nanoparticles to Metal–Organic Frameworks with Size and Location Control for Optimizing Catalytic Performance

Qi-Long Zhu,<sup>†</sup> Jun Li,<sup>†,‡</sup> and Qiang Xu<sup>\*,†,‡</sup>

<sup>†</sup>National Institute of Advanced Industrial Science and Technology (AIST), Ikeda, Osaka 563-8577, Japan

<sup>‡</sup>Graduate School of Engineering, Kobe University, Nada Ku, Kobe, Hyogo, Japan

## Supporting Information

**ABSTRACT:** AuNi alloy nanoparticles were successfully immobilized to MIL-101 with size and location control for the first time by double solvents method (DSM) combined with a liquid-phase concentration-controlled reduction strategy. When an overwhelming reduction approach was employed, the uniform 3D distribution of the ultrafine AuNi nanoparticles (NPs) encapsulated in the pores of MIL-101 was achieved, as demonstrated by TEM and electron tomographic measurements, which brings light to new opportunities in the fabrication of ultrafine non-noble metal-based NPs throughout the interior pores of MOFs. The ultrafine AuNi alloy NPs inside the mesoporous MIL-101 exerted exceedingly high activity for hydrogen generation from the catalytic hydrolysis of ammonia borane.

Over the past decade, noble metal nanocatalysts have been extensively investigated and exhibited a wide range of potential applications in the fields of energy conversion and storage, environmental remediation, drug research and chemical production.<sup>1</sup> However, the noble catalysts are too expensive to be widely applied in practical applications. To improve the catalytic performance and minimize the usage of noble metals, the synthesis of non-noble metal-based nanocatalysts is an important topic in heterogeneous catalysis.<sup>2</sup> Alloying a parent metal with a second metal offers numerous opportunities for modulating the electronic structures of catalysts and optimizing their catalytic performance.<sup>2</sup>

Metal–organic frameworks (MOFs) synthesized by assembling metal ions with organic ligands have recently emerged as a new class of porous materials for their amenability to design as well as fine-tunable and uniform pore structures.<sup>3</sup> Their distinct characteristics make them very promising for a variety of applications, including gas storage and separation, sensing, optics, drug delivery, and catalysis.<sup>4</sup> Recently, by serving as unique host matrices, the potential applications of MOFs can be extended further by encapsulating metal nanoparticles (MNPs) within the frameworks.<sup>5</sup> The development of this type of composite materials to elicit enhanced properties is of current interest.

General synthetic methods to embed MNPs in a MOF matrix entail the impregnation of metal precursors with various techniques, such as chemical vapor deposition, solution infiltration, and solid grinding, followed by reduction of the metal precursors to metal atoms.<sup>5,6</sup> MOFs have been utilized as

supports for MNPs since they provide powerful confinement effect to limit the growth of MNPs; however, the precursor compounds and products can actually diffuse out through the pores of the host to form the MNPs with aggregation on the external surface of MOFs. To circumvent the drawbacks, great efforts have been made. Recently, we developed a double solvent method which could greatly minimize the deposition of metal precursors on the outer surface.<sup>7</sup> When the noble metal precursors are loaded, they can be treated by the hydrogen and plasma reduction methods under relatively moderate conditions which are suited perfectly for the preparation of noble NPs hosted inside the MOFs,<sup>7,8</sup> but not for non-noble metal-based NPs because of contradictions between the high reduction temperatures of non-noble metals and the low thermal stabilities of MOFs. Therefore, a general and facile method that can easily control the nucleation and growth of MNPs, especially non-noble metal-based NPs, with high uniformity only inside the pores of MOF is still imperative.

Herein, we exploit a liquid-phase concentration-controlled reduction (CCR) strategy for the first time to control the size and location of the AuNi NPs during reduction of the  $\text{Au}^{3+}$  and  $\text{Ni}^{2+}$  precursors which are introduced into the pores of MOF by using the double solvents method (Figure 1). When an overwhelming reduction (OWR) approach with a high-concentration reductant solution is employed, ultrafine AuNi alloy NPs are successfully encapsulated into the MOF nanopores without aggregation on the external surface. In contrast, serious agglomeration of MNPs can occur if a

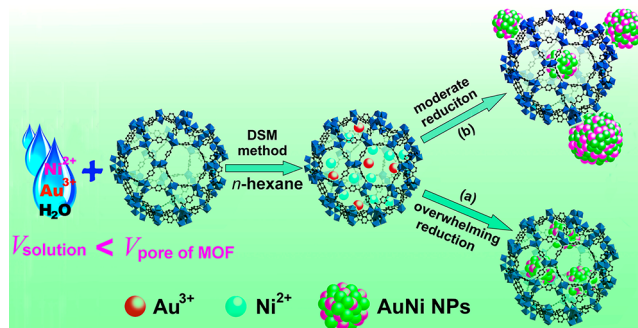


**Figure 1.** Schematic representation of immobilization of the AuNi nanoparticles by the MIL-101 matrix using the DSM combined with a liquid-phase CCR strategy.

Received: April 4, 2013

moderate reduction (MR) approach is chosen. The highly dispersed AuNi NPs in the MOF pores exhibit excellent catalytic performance in hydrolytic dehydrogenation of ammonia borane, one of the most attractive candidates for chemical hydrogen storage.<sup>9</sup>

MIL-101, a chromium-based MOF with molecular formula  $\text{Cr}_3\text{F}(\text{H}_2\text{O})_2\text{O}[(\text{O}_2\text{C})\text{C}_6\text{H}_4(\text{CO}_2)]_3\cdot n\text{H}_2\text{O}$  (where  $n = \sim 25$ ), was selected as a host matrix in this work to encapsulate metallic particles not only because of its incredibly large pore size (2.9 to 3.4 nm) and high specific surface area (Langmuir surface area reaches 5900 m<sup>2</sup>/g) but also because of its long-term stability in water and air atmospheres.<sup>10</sup> The pore windows with diameters of ~1.2 and 1.6 nm are big enough for the precursor compounds HAuCl<sub>4</sub> and NiCl<sub>2</sub> to diffuse into the pores, within which nucleation can take place to form the AuNi alloy NPs. The impregnation of metal precursors was conducted by using double solvents method in order to avoid the deposition of the precursors on the outer surface of MOF.<sup>7</sup> Because of the large inner surface area of MIL-101 with hydrophilic character derived from the metal-cluster based trimeric building block,<sup>4j</sup> the small amount of aqueous precursor solution, with a volume slightly less than the pore volume of the adsorbent, was readily incorporated into the pores of dehydrated MIL-101, which was suspended in a large amount of dry *n*-hexane, by capillary force. Since the inner surface area of MIL-101 is much larger than the outer surface area, the small amount of aqueous precursor solution can go inside the hydrophilic pore, and the deposition of metal precursors on the outer surface can be minimized. After loading the precursors and drying the metal precursor/MOF composite, an OWR approach with a high-concentration NaBH<sub>4</sub> solution was carried out for avoiding MNPs aggregation on external surfaces of MIL-101 framework, which is based on the assumption that when the metal precursors deposited in the pores of MOF can be reduced completely by a pore-volume amount of NaBH<sub>4</sub> solution that can be incorporated into the pores by capillary force, the aggregation of MNPs on the external surface will be avoided utmostly. Otherwise, when a low-concentration NaBH<sub>4</sub> solution was used, the reduction of the precursor inside the pores can not be completed, and a part of the precursors would be redissolved and diffuse out of the pores, resulting in the aggregation of MNPs on the outer surface of MOF. Thus, the control of size and location of MNPs can be achieved by using the CCR strategy, i.e., controlling the amount of the reductant in a certain volume of solution equal to the pore volume of MOF.

For preparing MNPs immobilized by MIL-101, activated MIL-101 (200 mg), which possesses a pore volume of 2.11 cm<sup>3</sup> g<sup>-1</sup> as determined by N<sub>2</sub> sorption isotherm, was suspended in *n*-hexane (40 mL), to which an aqueous metal precursor solution (0.36 mL) was added dropwise under vigorous stirring. After careful filtration, the synthesized samples were dehydrated at 150 °C, followed by reduction with various concentrations of NaBH<sub>4</sub>. The uniform MNPs throughout the interior pores of MIL-101 were achieved as the concentration of the aqueous NaBH<sub>4</sub> solution was increased to 0.6 M, which therefore was chosen as the critical concentration for the OWR approach. The catalytic activities for hydrolysis of ammonia borane were tested for the prepared samples.<sup>9</sup> Among the catalysts of AuNi@MIL-101 obtained by reduction with 0.6 M aqueous NaBH<sub>4</sub> solution, the catalyst with the Au/Ni atomic ratio of 7:93 exhibited the highest activity (*vide infra*), and therefore Au<sub>0.07</sub>Ni<sub>0.93</sub>@MIL-101 was chosen as the model catalyst to

explore the effect of the reductant concentration on the size and location of the MNPs with the CCR strategy. The resultant nanocomposites obtained by reduction using aqueous NaBH<sub>4</sub> solutions of 0.6, 0.4, and 0.2 M are denoted as AuNi@MIL-101\_a–c, respectively.

When a high-concentration NaBH<sub>4</sub> solution (0.6 M) is used, an OWR takes place to the precursors incorporated in the pores of MIL-101 (Figure 1), resulting in the formation of highly dispersed AuNi alloy NPs with average size of 1.8 ± 0.2 nm encapsulated within the pores of MIL-101 without deposition of the NPs on the external surface, which has been confirmed by the TEM, high-annular dark-field scanning TEM (HAADF-STEM), energy-dispersive X-ray spectroscopy (EDX) analyses and electron tomographic reconstruction (Figures 2a,b, S6 and S7 and a movie for AuNi@MIL-

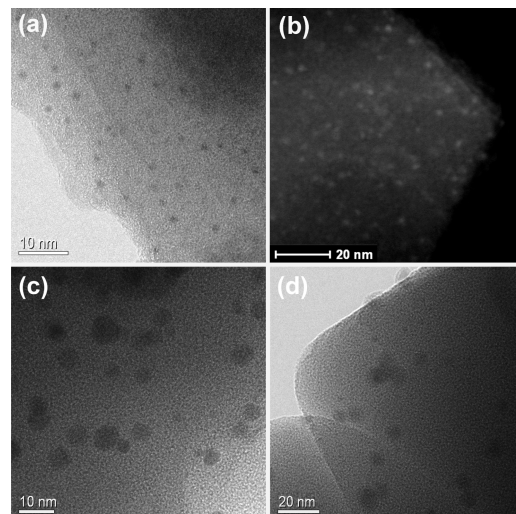


**Figure 2.** (a) TEM and (b) HAADF-STEM images of AuNi@MIL-101\_a; and TEM images of (c) AuNi@MIL-101\_b and (d) AuNi@MIL-101\_c.

101\_a).<sup>11</sup> The two kinds of mesoporous cavities of MIL-101 are large enough to accommodate the small MNPs. These TEM images showed no large particle aggregation, and the electron tomographic reconstruction definitely demonstrated the uniform 3D distribution of monodispersed AuNi NPs throughout the interior cavities of MIL-101 crystals. However, under MR conditions (Figure 1), agglomeration of larger MNPs on the external surface of MIL-101 was observed. In 0.4 M NaBH<sub>4</sub> solution, AuNi@MIL-101\_b with MNPs of 2.0–5.0 nm was obtained (Figure 2c), while in 0.2 M NaBH<sub>4</sub> solution, AuNi@MIL-101\_c was formed with most of the MNPs >5.0 nm (Figure 2d). These results indicate that, below the critical concentration of 0.6 M, the reductant in the solution within a volume equal to the pore volume of MOF is not enough to completely reduce the loaded metal precursors, and a part of the metal precursors incorporated within the pores redissolve into the solution and diffuse out of the pores, resulting in the agglomeration of MNPs on the external surface of MOF; the further the reductant concentration selected strays from the critical level, the more severe MNP agglomeration occurs. Consequently, the strategy employed here demonstrates that the combination of the double solvents method and the OWR approach can facilely and effectively control the capsulation of the MNPs into the pores of MIL-101, which can be easily

expanded to the other systems with different metal precursors and MOF matrices possessing hydrophilic pores.<sup>4</sup>

After the impregnation and reduction processes, there is no loss of the crystallinity in powder X-ray diffraction (PXRD) patterns for Au@MIL-101, Ni@MIL-101, and AuNi@MIL-101\_a–c, which are similar to the simulated pattern of MIL-101 reported by Férey et al,<sup>10</sup> indicating that the integrity of the MIL-101 framework is maintained (Figures S2 and S3). Moreover, no diffractions were detected for MNPs in M@MIL-101 obtained by reduction via the OWR approach, indicating the formation of very small MNPs. As the size of MNPs increases, the diffractions for the AuNi alloy phases between the characteristic peaks of Au(111) and Ni(111) were observable for the AuNi@MIL-101\_b and AuNi@MIL-101\_c samples.<sup>11,12</sup> The appreciable decreases in the surface areas and the pore volumes of M@MIL-101 indicate that the pores of the host frameworks are occupied by dispersed MNPs and/or blocked by the MNPs located on surface (Figure S4).<sup>11</sup> The X-ray photoelectron spectroscopic (XPS) investigation of AuNi@MIL-101\_a at the Au 4f and Ni 2p levels exhibits that metallic Au and Ni peak intensities changed synchronously during the Ar etching, indicating the homogeneity of the AuNi alloy particles (Figure S5).<sup>11</sup>

It is well-known that ammonia borane ( $\text{NH}_3\text{BH}_3$ , AB) is a promising material for chemical hydrogen storage,<sup>9</sup> from which hydrogen can be released through hydrolysis.<sup>13</sup> In this work, AB hydrolysis is employed for evaluating the catalytic activities of the M@MIL-101 catalysts. Reaction was initiated by introducing aqueous AB solution into the reaction flask containing the as-synthesized M@MIL-101 catalysts with vigorous shaking at room temperature.  $\text{H}_2$  generated from the AB hydrolysis was collected in the buret, with which the  $\text{H}_2$  volume was monitored. Figures 3 and S11 show the  $\text{H}_2$

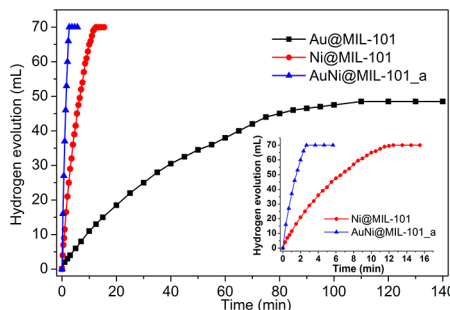


**Figure 3.** Plots of time vs volume of hydrogen generated from AB (1 mmol in 5 mL water) hydrolysis at room temperature catalyzed by the Au@MIL-101, Ni@MIL-101, and AuNi@MIL-101\_a catalysts (50 mg, (Au+Ni)/AB (molar ratio) = 0.017).

generation from aqueous AB in the presence of M@MIL-101 prepared by reduction using 0.6 M  $\text{NaBH}_4$  with various Au/Ni compositions.<sup>11</sup> It is revealed that the AuNi@MIL-101 catalysts are more active for the hydrolysis of AB than the monometallic counterparts, exhibiting synergistic effect between Au and Ni.<sup>2</sup> Under our evaluation conditions, the AuNi@MIL-101 with the Au/Ni atomic ratio of 7:93 is the most active, in which the AB hydrolysis reaction is completed in 2.67 min with a 70 mL  $\text{H}_2$  release, corresponding to  $\text{H}_2/\text{AB} = 3$  ((Au + Ni)/AB = 0.017 in molar ratio), giving a turnover frequency (TOF) value of  $66.2 \text{ mol}_{\text{H}_2} \cdot \text{mol}_{\text{cat}}^{-1} \cdot \text{min}^{-1}$ . This value is much higher than those of the most active non-noble metal-based catalysts for this reaction reported so far and even higher than those of most Pt, Rh and

Ru-related catalysts.<sup>9e,13</sup> Reasonably, the small sizes of surfactant-free AuNi NPs within MIL-101 and synergistic effect between Au and Ni account for the observed high catalytic activity. It is found that the productivity of  $\text{H}_2$  over the AuNi@MIL-101\_a catalyst almost remained unchanged after five runs, indicating the high durability in AB hydrolysis (Figure S12). Since the degenerative performance can be recovered totally after catalyst recycling, the slight activity drop should be attributed to the increase in concentration of metaborate ( $\text{BO}_2^-$ ) and the viscosity of the solution during the AB hydrolysis. Once metaborate generated during the reaction was removed from solution, the catalyst exhibited its original catalytic activity (Figure S12).<sup>11</sup> PXRD (Figure S14a,b) and TEM (Figures S15a,b) measurements of AuNi@MIL-101\_a after catalysis showed no significant change in the morphologies of AuNi NPs with retention of the MIL-101 framework.<sup>11</sup> Uniform distribution of AuNi alloy NPs without aggregation after catalysis confirms the advantage of the confinement effect of the MOF matrix.

It has been known that the catalytic activity generally increases with the decrease in MNP size, as smaller MNPs have higher surface areas available for reactants.<sup>14</sup> Thus, the effect of the size and location of the MNPs on its AB hydrolysis kinetics was further evaluated by using AuNi@MIL-101\_a–c, which were obtained by using the CCR reduction strategy. Figure 4

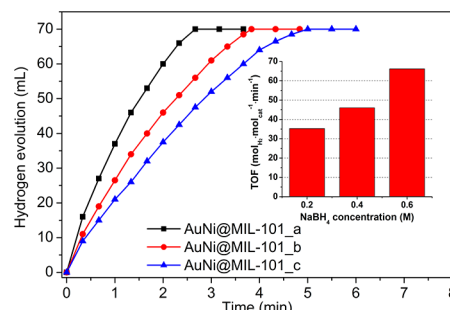


**Figure 4.** Plots of time vs volume of hydrogen generated from AB (1 mmol in 5 mL water) hydrolysis at room temperature catalyzed by the AuNi@MIL-101\_a–c catalysts (50 mg, (Au+Ni)/AB (molar ratio) = 0.017) prepared by reduction in  $\text{NaBH}_4$  solution with different concentrations. Inset: the corresponding TOF values of the catalysts.

shows the plots of time vs volume of  $\text{H}_2$  generated during AB hydrolysis catalyzed by AuNi@MIL-101\_a–c with different particle sizes and locations. Comparing with the AuNi NPs in AuNi@MIL-101\_a, the AuNi NPs in AuNi@MIL-101\_b and AuNi@MIL-101\_c exhibit larger sizes with different degrees of agglomeration on the external surface of MIL-101 crystals. Accordingly, their significant decreases in the TOF values from 66.2 to 46.0 and  $35.3 \text{ mol}_{\text{H}_2} \cdot \text{mol}_{\text{cat}}^{-1} \cdot \text{min}^{-1}$ , respectively, and in the initial dehydrogenation rates indicate that the catalytic activity is severely decreased with the increase of MNPs size (Figures 4 inset and S10). Furthermore, AuNi@MIL-101\_c features much lower durability in AB hydrolysis than that of AuNi@MIL-101\_a, which may be attributed to the lack of the pore confinement effect of MIL-101 to protect the MNPs from agglomeration (Figures S13, S15c,d).<sup>11</sup>

In summary, we have developed a facile and effective approach via a liquid-phase CCR strategy in combination with the DSM for the first time to control the size and location of the MOF-immobilized metal NPs, especially the non-noble metal-based NPs, which are difficult to be obtained by  $\text{H}_2$

reduction at a moderate temperature where MOFs can remain stable. When an OWR approach is employed, the incorporation of ultrafine MNPs within the pores of MOFs without agglomeration of the MNPs on the external surface of host framework is easily achieved. We have used this approach to fabricate ultrafine AuNi alloy NPs inside the mesoporous MIL-101, which could serve as a high-performance catalyst for future development of ammonia borane into a practical hydrogen storage materials for clean energy applications. The present results open up new avenues for developing high-performance heterogeneous catalysts by using porous MOFs as hosts for ultrafine metal NPs, especially non-noble metal-based NPs.

## ASSOCIATED CONTENT

### Supporting Information

Experimental procedures; PXRD, BET, XPS, TEM, EDX for catalysts; results of catalytic AB hydrolysis; durability and stability results of catalysts. This material is available free of charge via the Internet at <http://pubs.acs.org>.

## AUTHOR INFORMATION

### Corresponding Author

[q.xu@aist.go.jp](mailto:q.xu@aist.go.jp)

### Notes

The authors declare no competing financial interest.

## ACKNOWLEDGMENTS

The authors are thankful to the reviewers for valuable suggestions, Dr. Takeyuki Uchida and Dr. Tomoki Akita for TEM measurements and AIST and METI for financial support.

## REFERENCES

- (1) (a) Scott, R. W.; Wilson, O. M.; Oh, S.-K.; Kenik, E. A.; Crooks, R. M. *J. Am. Chem. Soc.* **2004**, *126*, 15583. (b) Guo, Y.-G.; Hu, J.-S.; Wan, L.-J. *Adv. Mater.* **2008**, *20*, 2878. (c) Zhang, H.; Jin, M.; Xia, Y. *Chem. Soc. Rev.* **2012**, *41*, 8035. (d) Hong, X.; Wang, D.; Cai, S.; Rong, H.; Li, Y. *J. Am. Chem. Soc.* **2012**, *134*, 18165.
- (2) (a) Bashyam, R.; Zelenay, P. *Nature* **2006**, *443*, 63. (b) Morozan, A.; Jousselme, B.; Palacin, S. *Energy Environ. Sci.* **2011**, *4*, 1238. (c) Jiang, H.-L.; Xu, Q. *J. Mater. Chem.* **2011**, *21*, 13705. (d) Singh, A. K.; Xu, Q. *ChemCatChem* **2013**, *5*, 652.
- (3) (a) Eddaoudi, M.; Kim, J.; Rosi, N.; Vodak, D.; Wachter, J.; O'Keeffe, M.; Yaghi, O. M. *Science* **2002**, *295*, 469. (b) Zhang, J.-P.; Huang, X.-C.; Chen, X.-M. *Chem. Soc. Rev.* **2009**, *38*, 2385. (c) Férey, G.; Serre, C. *Chem. Soc. Rev.* **2009**, *38*, 1380. (d) Yuan, D.; Zhao, D.; Sun, D.; Zhou, H.-C. *Angew. Chem., Int. Ed.* **2010**, *49*, 5357. (e) Chen, B.; Xiang, S.; Qian, G. *Acc. Chem. Res.* **2010**, *43*, 1115. (f) Wu, T.; Wang, L.; Bu, X.; Chau, V.; Feng, P. *J. Am. Chem. Soc.* **2012**, *134*, 4517.
- (4) (a) Ghosh, S. K.; Bureekaew, S.; Kitagawa, S. *Angew. Chem., Int. Ed.* **2008**, *47*, 3403. (b) Ma, S.; Zhou, H.-C. *J. Am. Chem. Soc.* **2006**, *128*, 11734. (c) Ma, L.; Jin, A.; Xie, Z.; Lin, W. *Angew. Chem., Int. Ed.* **2009**, *48*, 9905. (d) Lee, J.; Farha, O. K.; Roberts, J.; Scheidt, K. A.; Nguyen, S. T.; Hupp, J. T. *Chem. Soc. Rev.* **2009**, *38*, 1450. (e) He, Y.; Xiang, S.; Chen, B. *J. Am. Chem. Soc.* **2011**, *133*, 14570. (f) Motoyama, S.; Makiura, R.; Sakata, O.; Kitagawa, H. *J. Am. Chem. Soc.* **2011**, *133*, 5640. (g) Akiyama, G.; Matsuda, R.; Sato, H.; Takata, M.; Kitagawa, S. *Adv. Mater.* **2011**, *23*, 3294. (h) Shigematsu, A.; Yamada, T.; Kitagawa, H. *J. Am. Chem. Soc.* **2012**, *134*, 13145. (i) Wanderley, M. M.; Wang, C.; Wu, C.-D.; Lin, W. *J. Am. Chem. Soc.* **2012**, *134*, 9050. (j) Küsgens, P.; Rose, M.; Senkovska, I.; Fröde, H.; Henschel, A.; Siegle, S.; Kaskel, S. *Microporous Mesoporous Mater.* **2009**, *120*, 325.
- (5) (a) Cheon, Y. E.; Suh, M. P. *Chem.—Eur. J.* **2008**, *14*, 3961. (b) Park, Y. K.; Choi, S. B.; Nam, H. J.; Jung, D.; Ahn, H. C.; Choi, K.; Furukawa, H.; Kim, J. *Chem. Commun.* **2010**, *46*, 3086. (c) Lu, G.; Li, S.; Guo, Z.; Farha, O. K.; Hauser, B. G.; Qi, X.; Wang, Y.; Wang, X.; Han, S.; Liu, X.; DuChene, J. S.; Zhang, H.; Zhang, Q.; Chen, X.; Ma, J.; Loo, S. C. J.; Wei, W. D.; Yang, Y.; Hupp, J. T.; Huo, F. *Nat. Chem.* **2012**, *4*, 310. (d) Dhakshinamoorthy, A.; Garcia, H. *Chem. Soc. Rev.* **2012**, *41*, 5262. (e) Wang, C.; deKrafft, K. E.; Lin, W. *J. Am. Chem. Soc.* **2012**, *134*, 7211. (f) Moon, H. R.; Lim, D.-W.; Suh, M. P. *Chem. Soc. Rev.* **2013**, *42*, 1807. (g) Li, S.-L.; Xu, Q. *Energy Environ. Sci.* **2013**, *6*, 1656.
- (6) (a) Hermes, S.; Schröter, M.-K.; Schmid, R.; Khodeir, L.; Muhler, M.; Tissler, A.; Fischer, R. W.; Fischer, R. A. *Angew. Chem., Int. Ed.* **2005**, *44*, 6237. (b) Proch, S.; Herrmannsdörfer, J.; Kempe, R.; Kern, C.; Jess, A.; Seyfarth, L.; Senker, J. *Chem.—Eur. J.* **2008**, *14*, 8204. (c) Jiang, H.-L.; Akita, T.; Ishida, T.; Haruta, M.; Xu, Q. *J. Am. Chem. Soc.* **2011**, *133*, 1304. (d) Gu, X.; Lu, Z.-H.; Jiang, H.-L.; Akita, T.; Xu, Q. *J. Am. Chem. Soc.* **2011**, *133*, 11822.
- (7) Ajaz, A.; Karkamkar, A.; Choi, Y. J.; Tsumori, N.; Rönnebro, E.; Autrey, T.; Shioyama, H.; Xu, Q. *J. Am. Chem. Soc.* **2012**, *134*, 13926.
- (8) Zou, J.-J.; Zhang, Y.-p.; Liu, C.-J. *Langmuir* **2006**, *22*, 11388.
- (9) (a) Gutowska, A.; Li, L.; Shin, Y.; Wang, C. M.; Li, X. S.; Linehan, J. C.; Smith, R. S.; Kay, B. D.; Schmid, B.; Shaw, W.; Gutowski, M.; Autrey, T. *Angew. Chem., Int. Ed.* **2005**, *44*, 3578. (b) Keaton, R. J.; Blacquiere, J. M.; Baker, R. T. *J. Am. Chem. Soc.* **2007**, *129*, 1844. (c) Kim, S.-K.; Han, W.-S.; Kim, T.-J.; Kim, T.-Y.; Nam, S. W.; Mitoraj, M.; Piekos, L.; Michalak, A.; Hwang, S. J.; Kang, S. O. *J. Am. Chem. Soc.* **2010**, *132*, 9954. (d) Kim, S.-K.; Kim, T.-J.; Kim, T.-Y.; Lee, G.; Park, J. T.; Nam, S. W.; Kang, S. O. *Chem. Commun.* **2012**, *48*, 2021. (e) Yadav, M.; Xu, Q. *Energy Environ. Sci.* **2012**, *5*, 9698–9725.
- (10) Férey, G.; Mellot-Draznieks, C.; Serre, C.; Millange, F.; Dutour, J.; Surblé, S.; Margiolaki, I. *Science* **2005**, *309*, 2040.
- (11) See the Supporting Information.
- (12) Zhou, S.; Yin, H.; Schwartz, V.; Wu, Z.; Mullins, D.; Eichhorn, B.; Overbury, S. H.; Dai, S. *ChemPhysChem* **2008**, *9*, 2475.
- (13) (a) Yan, J.-M.; Zhang, X.-B.; Han, S.; Shioyama, H.; Xu, Q. *Angew. Chem., Int. Ed.* **2008**, *47*, 2287. (b) Metin, Ö.; Özkara, S.; Sun, S. *Nano Res.* **2010**, *3*, 676. (c) Yan, J.-M.; Zhang, X.-B.; Akita, T.; Haruta, M.; Xu, Q. *J. Am. Chem. Soc.* **2010**, *132*, 5326. (d) Sanyal, U.; Demirci, U. B.; Jagirdar, B. R.; Miele, P. *ChemSusChem* **2011**, *4*, 1731. (e) Li, P. Z.; Ajaz, A.; Xu, Q. *Angew. Chem., Int. Ed.* **2012**, *51*, 6753.
- (14) (a) Tsunoyama, H.; Sakurai, H.; Negishi, Y.; Tsukuda, T. *J. Am. Chem. Soc.* **2005**, *127*, 9374. (b) Liu, H.; Liu, Y.; Li, Y.; Tang, Z.; Jiang, H. *J. Phys. Chem. C* **2010**, *114*, 13362.

# **Supporting Information**

## **Immobilizing Metal Nanoparticles to Metal–Organic Frameworks with Size and Location Control for Optimizing Catalytic Performance**

Qi-Long Zhu,<sup>†</sup> Jun Li<sup>‡‡</sup> and Qiang Xu<sup>††\*</sup>

<sup>†</sup>*National Institute of Advanced Industrial Science and Technology (AIST), Ikeda, Osaka 563-8577, Japan*

<sup>‡</sup>*Graduate School of Engineering, Kobe University, Nada Ku, Kobe, Hyogo, Japan*

### **1. Chemicals**

All chemicals were commercial and used without further purification. Chromic nitrate nonahydrate ( $\text{Cr}(\text{NO}_3)_3 \cdot 9\text{H}_2\text{O}$ , Sigma-Aldrich, 99%), aqueous hydrofluoric acid (HF, Kishida Chemical Co. Ltd., 46%), hydrogen tetrachloroaurate(III) tetrahydrate ( $\text{HAuCl}_4 \cdot 4\text{H}_2\text{O}$ , Wako Pure Chemical Industries, Ltd., >99%), nickel (II) chloride hexahydrate ( $\text{NiCl}_2 \cdot 6\text{H}_2\text{O}$ , Wako Pure Chemical Industries, Ltd., >98%), sodium borohydride ( $\text{NaBH}_4$ , Aldrich, 99%), ammonia borane ( $\text{NH}_3\text{BH}_3$ , JSC Aviabor, >97%), terephthalic acid ( $\text{HO}_2\text{CC}_6\text{H}_4\text{CO}_2\text{H}$ , Tri Chemical Laboratories Inc., 99%), anhydrous n-hexane (Sigma-Aldrich) and ethanol ( $\text{C}_2\text{H}_5\text{OH}$ , Kishida Chem. Co., >99.8%), were used as received. De-ionized water with a specific resistance of 18.2 MΩ·cm was obtained by reverse osmosis followed by ion-exchange and filtration (RFD 250NB, Toyo Seisakusho Kaisha, Ltd., Japan).

## 2. Syntheses of Catalysts

Metal nanoparticles (MNPs) were immobilized into the pores of MIL-101 with size and location control by double solvents method (DSM) combined with a liquid-phase concentration-controlled reduction (CCR) strategy (Figure S1).

**2.1 Synthesis of MIL-101:** MIL-101 was synthesized using the reported procedure.<sup>1</sup> Terephthalic acid (1.661 g, 10.0 mmol), Cr(NO<sub>3</sub>)<sub>3</sub>·9H<sub>2</sub>O (4.002 g, 10.0 mmol), aqueous HF (0.5 mL, 46 wt%) and de-ionized water (70 mL) were placed in a 100 mL Teflon-liner autoclave and heated at 220 °C for 8 h. After natural cooling, the resulting green powder of MIL-101 with formula Cr<sub>3</sub>F(H<sub>2</sub>O)<sub>2</sub>O[(O<sub>2</sub>C)C<sub>6</sub>H<sub>4</sub>(CO<sub>2</sub>)]<sub>3</sub>·nH<sub>2</sub>O ( $n \leq 25$ ) was doubly filtered off using two glass filters with pore sizes of 40 µm to eliminate the unreacted crystals of terephthalic acid, and then further purified by solvothermal treatment in ethanol at 100 °C for 24 h for twice and washed with hot ethanol. The resulting green solid was finally dried overnight at 150 °C under vacuum for further use.

**2.2 Syntheses of Au<sup>3+</sup>@MIL-101, Ni<sup>2+</sup>@MIL-101 and Au<sup>3+</sup>Ni<sup>2+</sup>@MIL-101:** Encapsulation of Au<sup>3+</sup> and Ni<sup>2+</sup> precursors was carried out using double solvents method.<sup>2</sup> Typically, 200 mg of dehydrated MIL-101 was suspended in 40 mL of dry *n*-hexane as hydrophobic solvent and the mixture was sonicated for about 20 min until it became homogeneous. After stirring for a while, 0.36 mL of aqueous HAuCl<sub>4</sub>·4H<sub>2</sub>O and/or NiCl<sub>2</sub>·6H<sub>2</sub>O solution with desired concentrations as the hydrophilic solvent was added dropwise over a period of 20 min with constant vigorous stirring. The resulting solution was continuously stirred for 3 h. After stirring, the solid which settled down to the bottom of the sample vial was isolated from the supernatant by decanting and drying in air at room temperature. The synthesized sample was further dried at 150 °C under vacuum for 12 h. The molar ratios of Au<sup>3+):(Au<sup>3+</sup> + Ni<sup>2+</sup>) were change with several values (0, 0.03, 0.05, 0.07, 0.10, 0.15, 0.30, 0.50 and 1.00), while the molar contents of (Au<sup>3+</sup> + Ni<sup>2+</sup>) added to 200 mg MIL-101 matrix were kept to be 0.068 mmol.</sup>

**2.3 Syntheses of Au@MIL-101, Ni@MIL-101 and AuNi@MIL-101:** The reduction of the catalysts was carried out using an overwhelming reduction (OWR) approach with 0.6 M aqueous NaBH<sub>4</sub> solution. In a typical experiment, after dehydration of the Au<sup>3+</sup>Ni<sup>2+</sup>@MIL-101 with different molar ratios of Au<sup>3+</sup> to Ni<sup>2+</sup>, 5 mL freshly prepared 0.6 M aqueous NaBH<sub>4</sub> solution was added while vigorous stirring, resulting in the generation of catalysts as a dark green suspension. The synthesized samples were collected by centrifuging, dried at 100 °C under vacuum, and used for the catalytic reactions. Analogous synthetic procedures were followed as those for bimetallic AuNi@MIL-101 catalysts to prepare the monometallic Au@MIL-101 and Ni@MIL-101 catalysts.

**2.4 Syntheses of AuNi@MIL-101\_a, AuNi@MIL-101\_b and AuNi@MIL-101\_c:** The control of size and location of the alloy NPs was exploited utilizing a liquid-phase concentration-controlled reduction strategy during the reduction of AuNi@MIL-101. To the dehydrated Au<sup>3+</sup>Ni<sup>2+</sup>@MIL-101

with the molar ratio of  $\text{Au}^{3+}:(\text{Au}^{3+} + \text{Ni}^{2+}) = 7:93$ , 5 mL freshly prepared 0.6, 0.4 and 0.2 M aqueous  $\text{NaBH}_4$  solutions were added while vigorous stirring, resulting in the generation of catalysts which were denoted as  $\text{AuNi@MIL-101\_a}$ ,  $\text{AuNi@MIL-101\_b}$  and  $\text{AuNi@MIL-101\_c}$ , respectively.

For encapsulating MNPs into the framework of MIL-101, the hydrophobic solvent is used for dispersing MIL-101 solid. 40 mL of n-hexane, which is enough to fully disperse the solid of MIL-101 (200 mg), was used in this work. As for the amount of precursor solution, a volume slightly less than the pore volume of MIL-101, which is determined by  $\text{N}_2$  sorption measurement, was used to incorporate the precursor inside the channels of host framework and minimize the deposition of precursor on the outer surface.

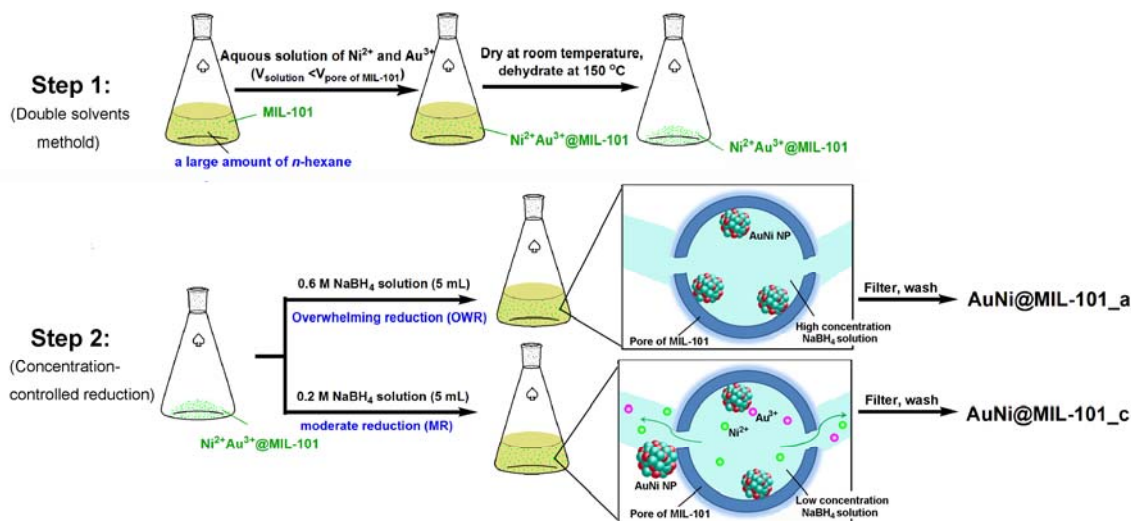


**Figure S1.** Diagram for the formation of  $\text{AuNi@MIL-101\_a}$  and  $\text{AuNi@MIL-101\_c}$ .

### 3. Physical Characterization for Catalysts

**3.1 Powder X-ray Diffraction (PXRD) Analyses:** Laboratory powder X-ray diffraction patterns were collected for synthesized MIL-101, Au@MIL-101, Ni@MIL-101 and AuNi@MIL-101\_a–c on a Rigaku RINT-2000 X-ray diffractometer with Cu K $\alpha$  source (40 kV, 40 mA). As shown in Figures S2 and S3, the powder X-ray diffraction patterns of the synthesized MIL-101, Au@MIL-101, Ni@MIL-101 and AuNi@MIL-101\_a–c are similar to the simulated patterns of reported MIL-101. All of them are of high crystallinity, indicating that the processes of encapsulation and reduction do not decrease the integrity of the MIL-101 framework. The sharp and strong peaks at 2–4° reveal the presence of both micropores and mesopores.<sup>1</sup> No diffractions were detected for MNPs in M@MIL-101 obtained by using the overwhelming reduction approach, indicating the formation of very small MNPs. As the size of MNPs increases, the diffractions for the AuNi alloy NPs in the AuNi@MIL-101\_b and AuNi@MIL-101\_c samples can be identified between the characteristic peaks of fcc Au (38.2°) and fcc Ni (44.5°).<sup>3</sup>

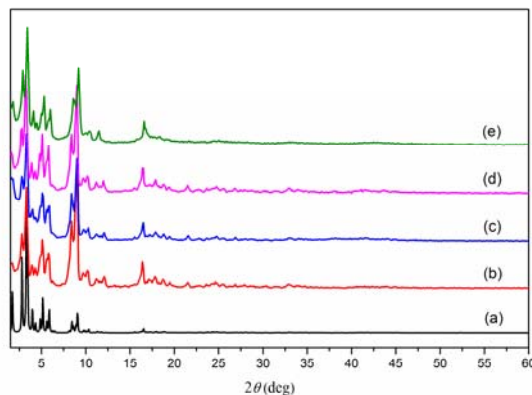


**Figure S2.** PXRD patterns of (a) simulated MIL-101, as-synthesized (b) MIL-101, (c) Au@MIL-101, (d) Ni@MIL-101 and (e) AuNi@MIL-101\_a.

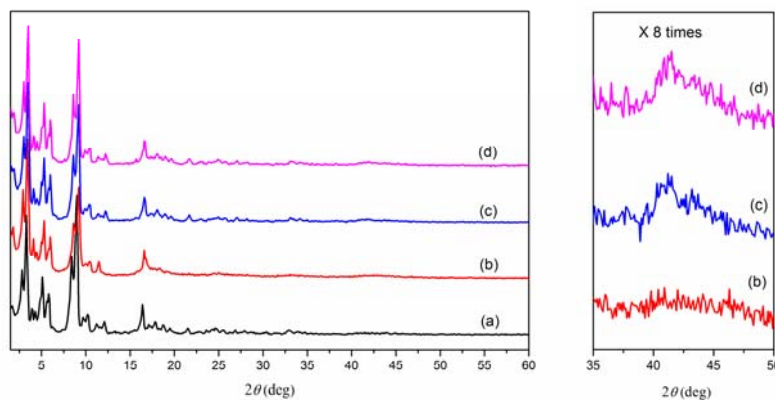


**Figure S3.** PXRD patterns of as-synthesized (a) MIL-101, (b) AuNi@MIL-101\_a, (c) AuNi@MIL-101\_b and (d) AuNi@MIL-101\_c. Enlargements ( $\times 8$  times of original intensity) of the region of  $2\theta = 35\text{--}50^\circ$  are shown on the right side.

**3.2 Nitrogen Sorption Measurements:** The surface area measurements were performed with N<sub>2</sub> adsorption/desorption isotherms at liquid nitrogen temperature (77 K) after dehydration under vacuum at 150 °C for 12 h using automatic volumetric adsorption equipment (Belsorp-max). The pore volume was calculated by a single point method at  $P/P_0 = 0.99$ . N<sub>2</sub> sorption isotherms of all samples shown in Figure S4 are of type I model with secondary uptakes at 0.0–0.02 and 0.21–0.24 of  $P/P_0$ , which is the characteristic of two kinds of microporous windows.<sup>1</sup> The BET surface areas of MIL-101, Ni@MIL-101, Au@MIL-101, AuNi@MIL-101\_a, AuNi@MIL-101\_b and AuNi@MIL-101\_c are 3193, 2347, 2220, 2277, 2451 and 2403 m<sup>2</sup>/g, respectively, and their Langmuir surface areas are 4647, 3533, 3367, 3436, 3708 and 3611 m<sup>2</sup>/g, respectively, and their pore volumes are 2.1093, 1.4963, 1.4180, 1.4652, 1.5403 and 1.5254 cm<sup>3</sup> g<sup>-1</sup>, respectively, as determined by N<sub>2</sub> sorption isotherms. The decreases of surface areas should be attributed to the incorporation of MNPs into the pores of MIL-101 and/or the block of MNPs located on framework surface of MIL-101.

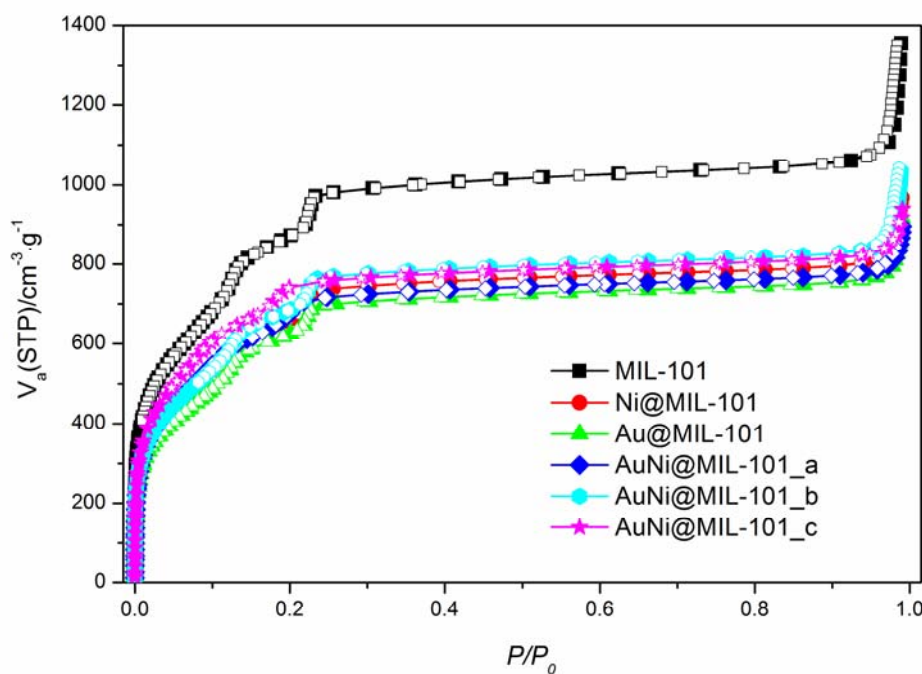


**Figure S4.** N<sub>2</sub> sorption isotherms of as-synthesized MIL-101, Ni@MIL-101, Au@MIL-101, AuNi@MIL-101\_a, AuNi@MIL-101\_b and AuNi@MIL-101\_c at 77 K. Filled and open symbols represent adsorption and desorption branches, respectively.

**3.3 X-ray Photoelectron Spectroscopic (XPS) Measurements:** XPS investigations were conducted for Au@MIL-101, Ni@MIL-101 and the representative AuNi@MIL-101\_a on a Shimadzu ESCA-3400 X-ray photoelectron spectrometer using an Mg K $\alpha$  source (10 kV, 10 mA). The argon sputtering experiments were carried out under the conditions of background vacuum of  $3.2 \times 10^{-6}$  Pa and sputtering acceleration voltage of 2 kV and sputtering current of 10 mA. Figure S5 shows the XPS spectra for the as-synthesized Au@MIL-101, Ni@MIL-101 and AuNi@MIL-101\_a at the Au 4f and Ni 2p levels. Well-defined peaks corresponding to metallic Au and Ni species both can be detected after Ar etching for 60 min, suggesting both of two elements are in their zero-valent states. The observed Au 4f<sub>7/2</sub> and Au 4f<sub>5/2</sub> binding energies at 83.8 and 87.5 eV correspond to Au<sup>0</sup>, and the Ni 2p<sub>3/2</sub> and Ni 2p<sub>1/2</sub> binding energies at 853.5 and 870.7 eV correspond to Ni<sup>0</sup>. A thin oxidized cover formed during the exposure of Ni@MIL-101 and AuNi@MIL-101\_a to air was observed at binding energies 858.5 and 875.8 eV for Ni 2p<sub>3/2</sub> and Ni 2p<sub>1/2</sub>, respectively, which was readily removed by Ar etching. The intensities of the metallic Au and Ni peaks change synchronously before and after Ar etching in AuNi@MIL-101\_a, indicating the homogenous alloy structure.

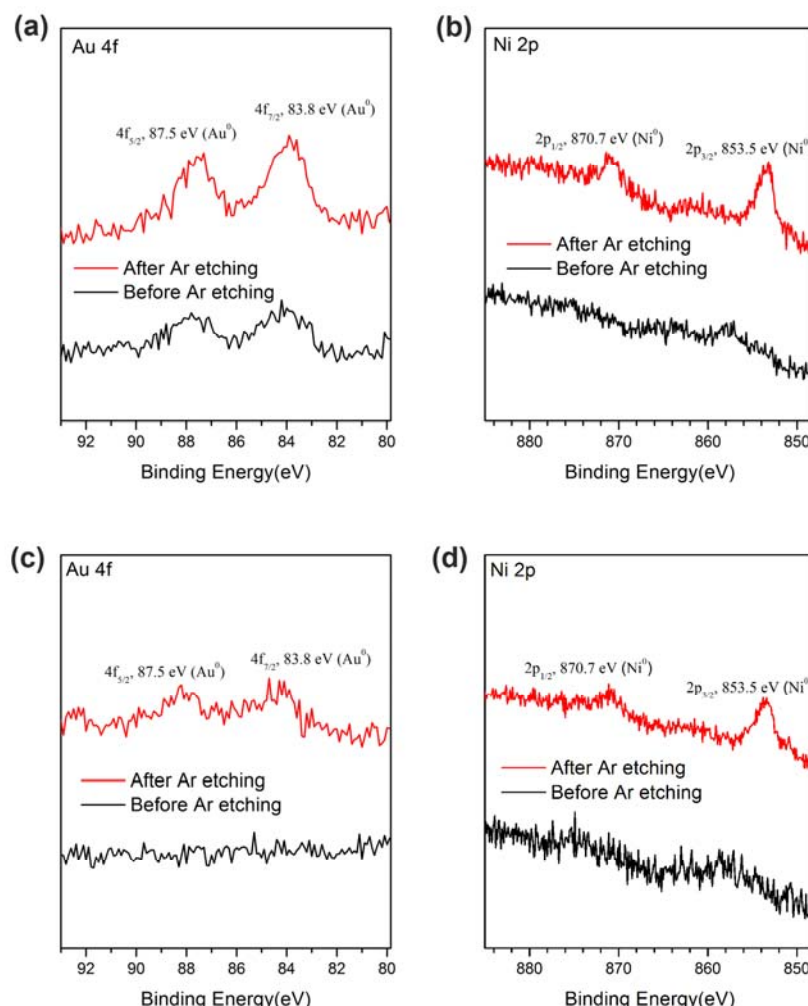


**Figure S5.** XPS spectra for (a) Au@MIL-101, (b) Ni@MIL-101, and (c, d) AuNi@MIL-101\_a before and after Ar etching for 60 min (Au 4f<sub>7/2</sub> and 4f<sub>5/2</sub> peaks, and Ni 2p<sub>3/2</sub> and 2p<sub>1/2</sub> peaks).

**3.4 TEM and EDX Analyses:** TEM and HAADF-STEM images and EDX spectrum were recorded on Transmission electron microscope (TEM, TECNAI G<sup>2</sup> F20 with operating voltage at 120 kV for AuNi@MIL-101\_a-c and FEI Titan3<sup>TM</sup> G2 60-300 with operating voltage at 300 kV for Ni@MIL-101, respectively) equipped with energy-dispersive X-ray detector (EDX). Tomographic experiments were performed using a tomography tilt stage and holder operated at 200 kV with punctual resolution 0.18 nm. Images for tomographic reconstruction were acquired from -30° to +30° with the tilt angle interval of 3°. A reference image taken at 0° tilt was taken before and after image acquisition to ensure no changes in the sample structure due to beam damage during acquisition. The three-dimensional (3D) structure information was reconstructed using the HAADF-STEM tomography images by the INSPECT 3D software package. Figures S6c-d show two 2D projection images of AuNi@MIL-101\_a on 0 ° and 24° from the tilt series by 3D tomography, while for the full 3D picture the readers can view an animation in the Supporting Information on the ACS web site. The HAADF-STEM images in Figure S9 also show the uniform distribution of ultrafine Ni NPs inside the pores of MIL-101.

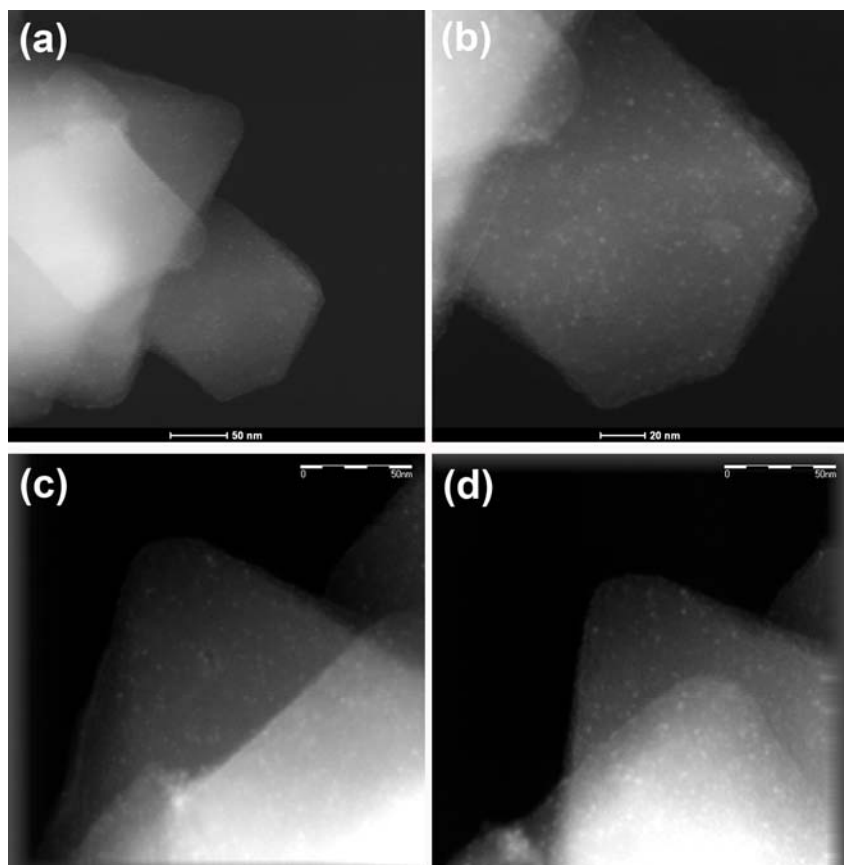


**Figure S6.** (a,b) HAADF-STEM images and (c,d) HAADF-STEM projection images on 0 ° and 24° from the tilt series by 3D tomography of AuNi@MIL-101\_a.

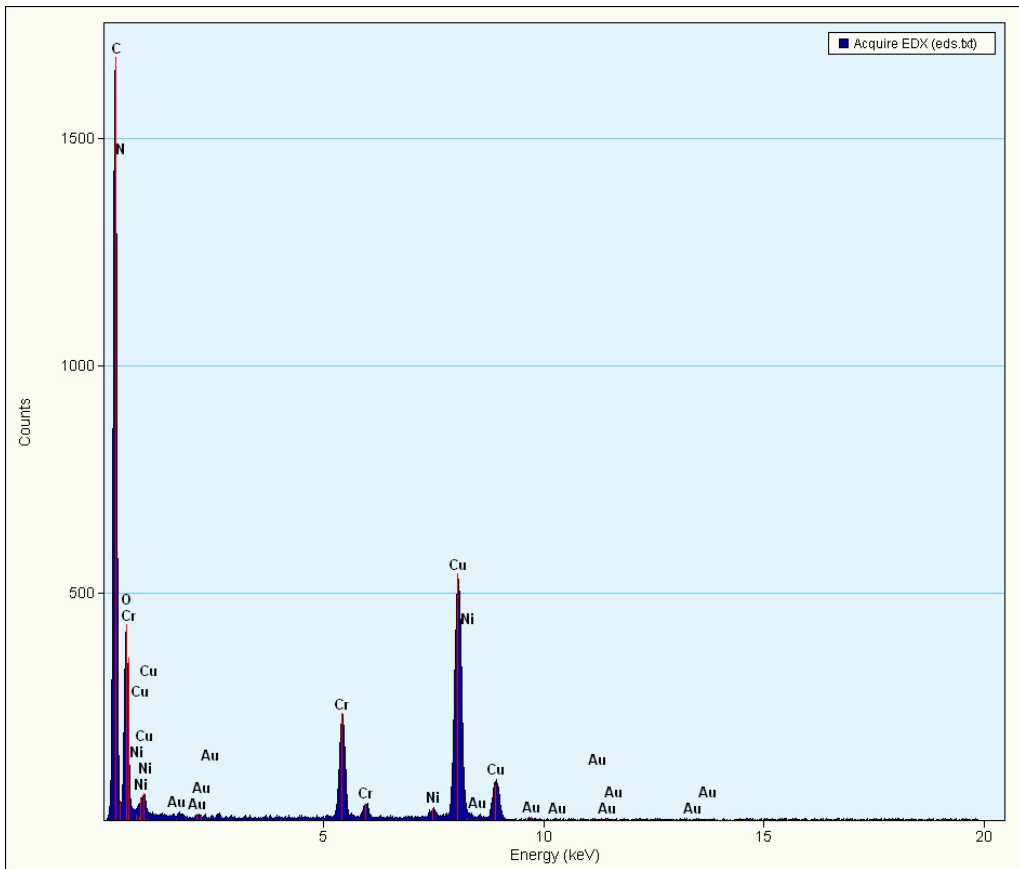


**Figure S7.** EDX pattern of bulk AuNi@MIL-101\_a from TEM measurement. The copper signal originates from Cu grid.

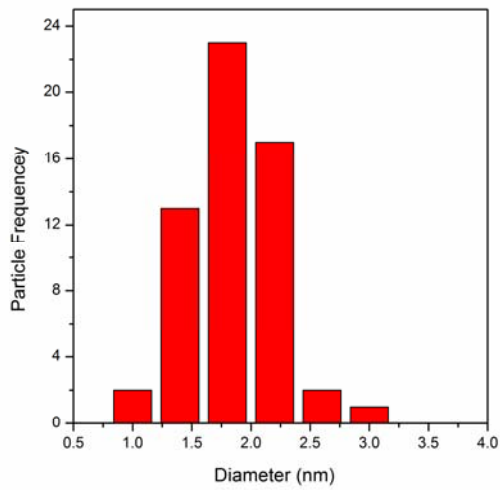


**Figure S8.** Size distribution of AuNi alloy nanoparticles in AuNi@MIL-101\_a sample.

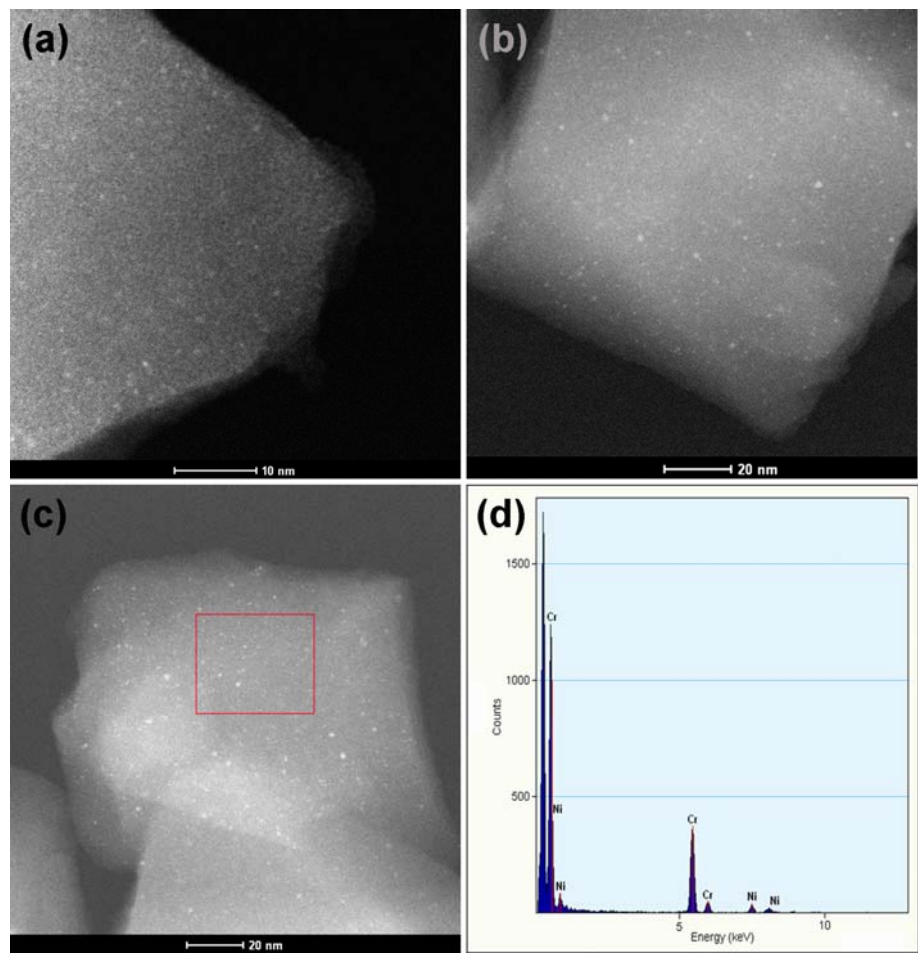


**Figure S9.** (a-c) HAADF-STEM images of Ni@MIL-101 and (d) the corresponding EDX spectrum of selected area in (c).

#### 4. Catalytic Activity Characterization

**4.1 Procedure for the Hydrolysis of Ammonia Borane:** Reaction apparatus for measuring the hydrogen evolution from the aqueous  $\text{NH}_3\text{BH}_3$  solution is the same as previously reported.<sup>4</sup> In general, a mixture of catalyst (50 mg) and distilled water (4 mL) was placed in a two-necked round-bottomed flask (30 mL), which was placed in a water bath at room temperature under ambient atmosphere. A gas burette filled with water was connected to the reaction flask to measure the volume of hydrogen. The reaction started when aqueous  $\text{NH}_3\text{BH}_3$  solution (1 mmol in 1 mL water) was injected into the mixture using a syringe. The volume of the evolved hydrogen gas was monitored by recording the displacement of water in the gas burette. The reaction was completed when there was no more gas generation. In addition, the molar ratios of  $(\text{Au}+\text{Ni})/\text{AB}$  were theoretically fixed at 0.017 for all the catalytic reactions, corresponding to 50 mg catalysts. The hydrolysis of  $\text{NH}_3\text{BH}_3$  can be briefly expressed as follows:



The hydrogen generations from the hydrolysis of aqueous AB catalyzed by the monometallic Au@MIL-101 and Ni@MIL-101 were shown in Figure 3 in the main text. Figure S10 exhibits the initial dehydrogenation rates of AuNi@MIL-101\_a-c estimated from the average rate at half completion of the reaction according to the Figure 4, indicative of that the catalytic activity greatly depends on the size and location of AuNi NPs. Figure S11a shows hydrogen generations from AB catalyzed by the synthesized AuNi@MIL-101 with different Au molar contents. It is clear that, compared to monometallic Ni and Au catalysts, the alloy structure significantly improves the catalytic activity. The dependence of the reaction time on the molar ratio of Au is in a shallow “V” shape (Figure S11b). That is, the reaction time first decreases with the increase of the Au content and reaches the minimum at 0.07 (reaction time: 2.67 min). Then, when the Au content further increases to 0.50, the tendency reverses and the reaction time is prolonged to 4 min. Based on the above results, the optimized molar ratio of Au to  $(\text{Au}+\text{Ni})$  is 0.07 for this reaction.

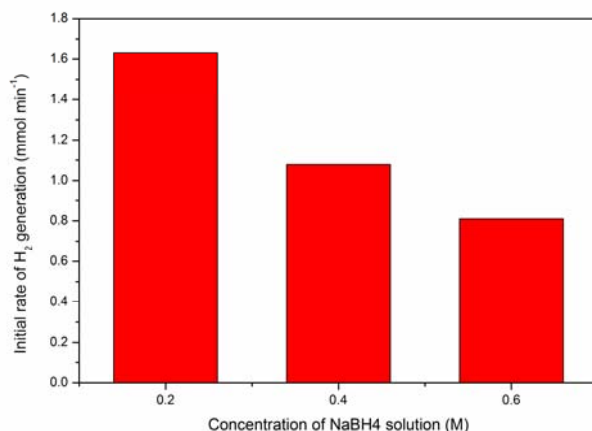


**Figure S10.** Initial dehydrogenation rate in the presence of AuNi@MIL-101\_a-c prepared by reduction in  $\text{NaBH}_4$  solution with different concentrations.

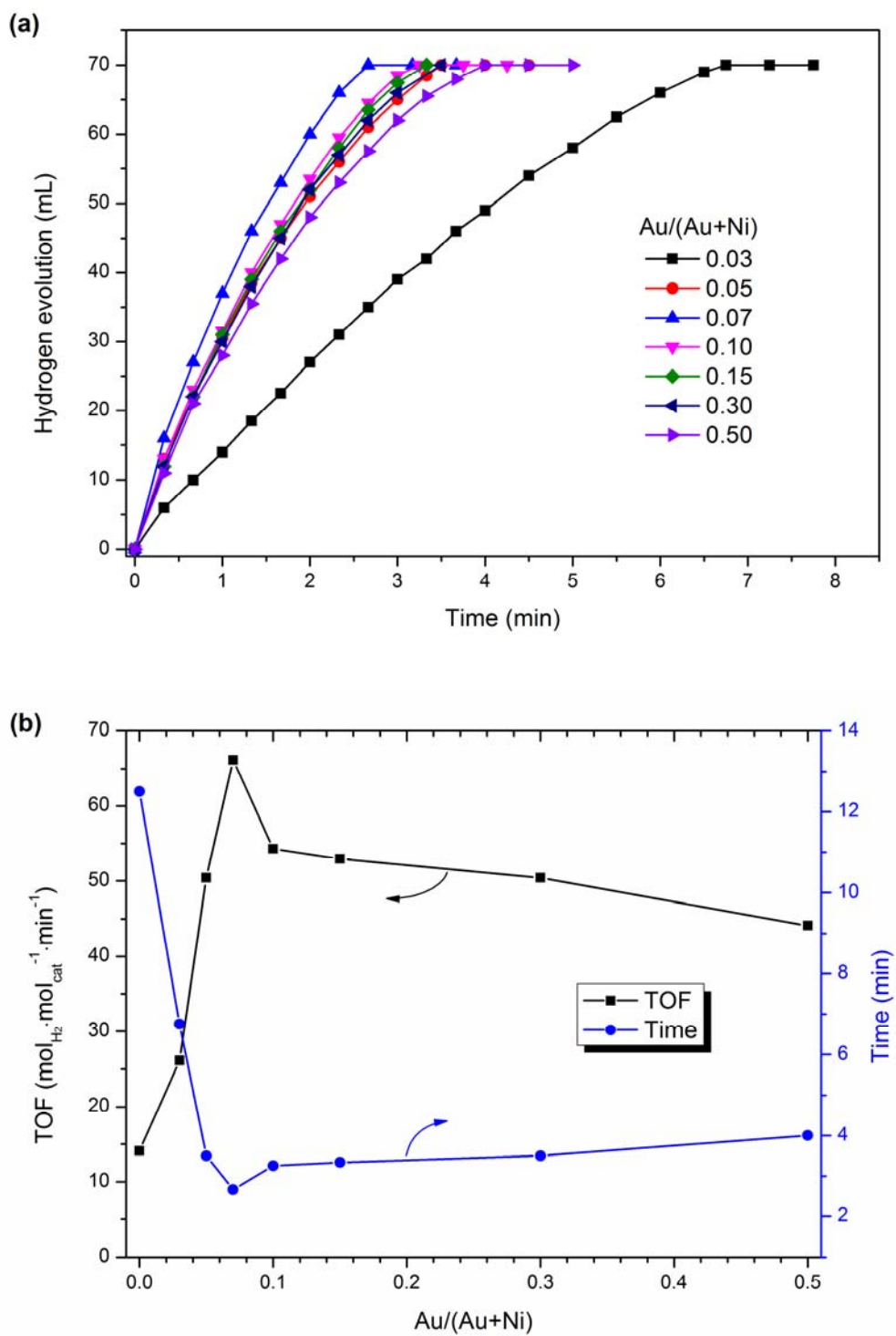


**Figure S11.** (a) Plots of time versus volume of hydrogen generated from AB (1.0 mmol in 5 mL H<sub>2</sub>O) by AuNi@MIL-101 catalysts with different Au molar contents, and (b) plots of time for reaction completion and the corresponding TOF value versus Au molar content in AuNi@MIL-101 ((Au+Ni)/AB=0.017).

**4.2 Durability Testing of the Catalysts:** For testing the durability of the catalysts, an aliquot of AB in 1 mL water was subsequently added into the reaction flask after the completion of the last run. Such test cycles of the catalyst for the hydrolysis of AB were carried out 5 runs at room temperature. After the reaction, the catalysts were recycled from the reaction solution by centrifugation and washing twice, and used again for the hydrolysis of AB under the same condition.

As shown in Figure S12, the AuNi@MIL-101\_a catalyst shows almost no activity loss in the five-cycle durability test. In addition, by recycling of this catalyst to remove the metaborate ( $\text{BO}_2^-$ ) generated during the AB hydrolysis, the slight activity drop was eliminated. However, in the case of AuNi@MIL-101\_c catalyst, more than half of the catalytic efficiency missed during the five runs. Even after recycling, the catalytic activity only recovered to 53% of the original level (Figure S13).

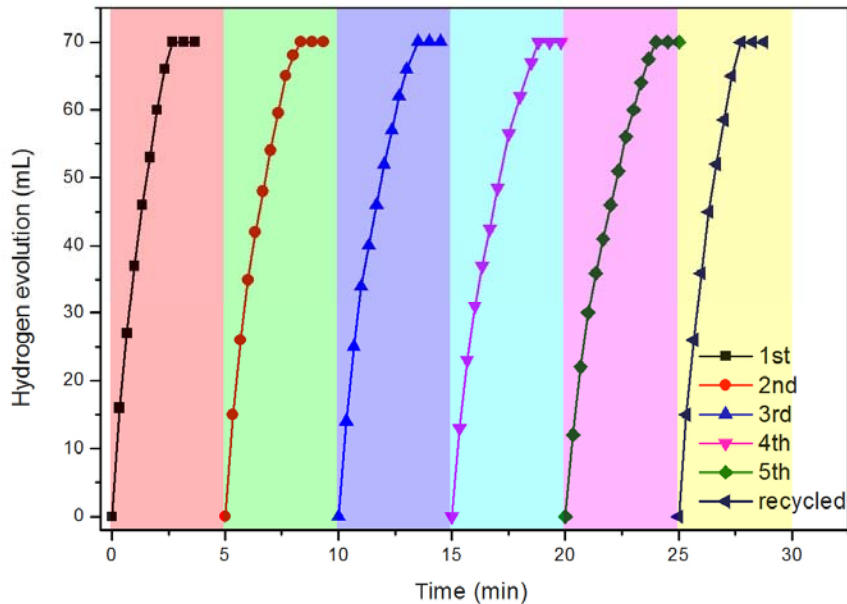


**Figure S12.** Durability test for the hydrogen generation from aqueous AB solution (1.0 mmol, 5.0 mL) catalyzed by AuNi@MIL-101\_a ((Au+Ni)/AB=0.017). Additional aliquots of AB in 1 mL water were added into the reaction flask after the completion of the last run. After five runs, the catalyst was recycled from the reaction solution and used again under the same catalytic condition.

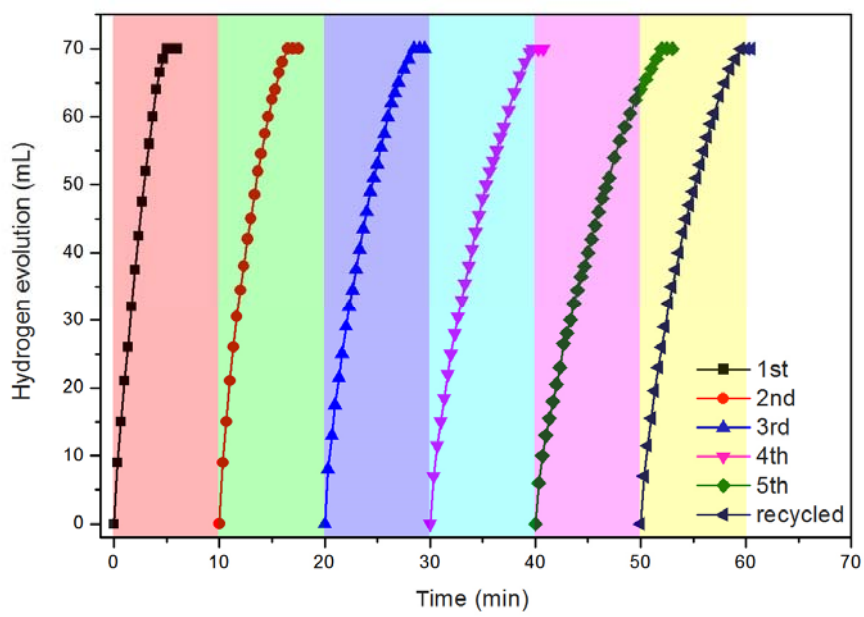


**Figure S13.** Durability test for the hydrogen generation from aqueous AB solution (1.0 mmol, 5.0 mL) catalyzed by AuNi@MIL-101\_c ((Au+Ni)/AB=0.017). Additional aliquots of AB in 1 mL water were added into the reaction flask after the completion of the last run. After five runs, the catalyst was recycled from the reaction solution and used again under the same catalytic condition,

**4.3 Stability of the Catalysts:** After the reaction, the catalysts were separated from the reaction solution by centrifugation and dried under vacuum at room temperature for characterization. The obtained samples before and after AB hydrolysis were used for the PXRD and TEM analyses.

As shown in Figure S14, the PXRD patterns of both AuNi@MIL-101\_a and AuNi@MIL-101\_c before and after catalysis exhibited that the main diffractions were well consistent with those of pristine MIL-101, indicating that the frameworks of MIL-101 were maintained well in the whole process of catalytic hydrolysis of AB.

The TEM images of AuNi@MIL-101\_a after catalysis (Figures S15a, b) prove that there is no significant change in AuNi NP size or morphology during catalytic reaction. It demonstrates the excellent confinement effect of the pores of MIL-101, which prevents the MNPs incorporated inside the pores from aggregation during the catalytic reaction. On the other hand, due to the fact that most of the NPs are located on the external s

urface of MIL-101 crystals, the TEM images of AuNi@MIL-101\_c after catalysis show that further agglomeration has occurred (Figures S15c, d). Thus, the difference in catalytic durability between AuNi@MIL-101\_a and AuNi@MIL-101\_c should be attributed to their different NP sizes and locations.

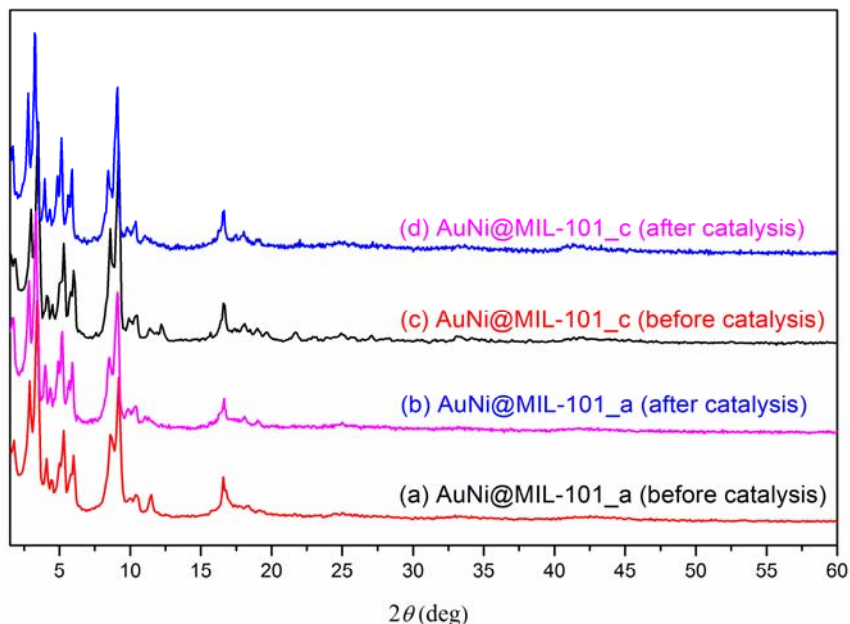


**Figure S14.** PXRD patterns of (a, b) AuNi@MIL-101\_a and (c, d) AuNi@MIL-101\_c before and after AB hydrolysis, respectively.

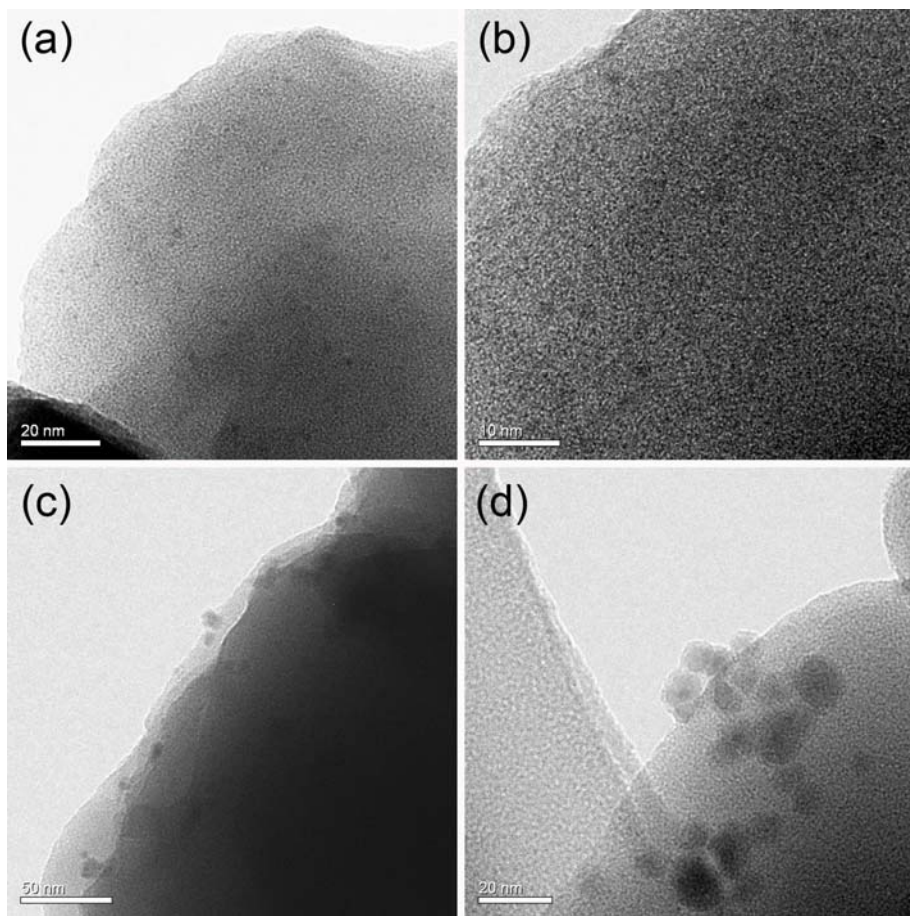


**Figure S15.** TEM images of (a,b) AuNi@MIL-101\_a and (c,d) AuNi@MIL-101\_c after AB hydrolysis.

## 5. References

- (1) Férey, G.; Mellot-Draznieks, C.; Serre, C.; Millange, F.; Dutour, J.; Surblé, S.; Margiolaki, I. *Science* **2005**, *309*, 2040.
- (2) Aijaz, A.; Karkamkar, A.; Choi, Y. J.; Tsumori, N.; Ronnebro, E.; Autrey, T.; Shioyama, H.; Xu, Q. *J. Am. Chem. Soc.* **2012**, *134*, 13926.
- (3) Zhou, S.; Yin, H.; Schwartz, V.; Wu, Z.; Mullins, D.; Eichhorn, B.; Overbury, S. H.; Dai, S. *ChemPhysChem* **2008**, *9*, 2475.
- (4) Chandra, M.; Xu, Q. *J. Power Sources* **2006**, *156*, 190.